IEEE Access
Multidisciplinary ⋮ Rapid Review ⋮ Open Access Journal

Received 31 December 2023, accepted 3 January 2024, date of publication 9 January 2024,
date of current version 18 January 2024.

Digital Object Identifier 10.1109/ACCESS.2024.3351811

RESEARCH ARTICLE

Zero Voltage Switching for High Power Three-Phase Inductive Power Transfer With a Dual Active Bridge

CHAO CUI[1,2,3], DANIEL PEHRMAN[2], (Student Member, IEEE), YUJING LIU[2], (Senior Member, IEEE), AND QIANFAN ZHANG[1,3], (Member, IEEE)

[1]School of Electrical Engineering and Automation, Harbin Institute of Technology, Harbin 150001, China
[2]Department of Electrical Engineering, Chalmers University of Technology, 412 96 Gothenburg, Sweden
[3]Zhengzhou Research Institute, Harbin Institute of Technology, Zhengzhou 450000, China

Corresponding author: Chao Cui (cuichao@hit.edu.cn)

This work was supported by the China Scholarship Council under Grant 201906120216.

ABSTRACT Inductive power transfer (IPT) technology used for charging electric vehicles faces challenges in transferring high power because the power capacity and switching losses of high-frequency semiconductor devices are limiting factors. A three-phase system is a common high-power solution and soft switching is crucial for efficiency-oriented applications with high switching frequencies. In addition, dual active bridge (DAB) topology is a suitable topology for soft switching and has advantages in controllability and high efficiency. Therefore, to obtain higher power and efficiency, this paper studies the zero voltage switching (ZVS) of a three-phase inductive power transfer system with a dual active bridge. The three-phase IPT system with a DAB is different from both the normal three-phase DAB converter and the single-phase IPT system with a DAB, so their ZVS conditions and ranges are also different and need to be studied. This paper investigates the conditions and operating range for realizing zero voltage switching of the three-phase IPT system with a DAB. Based on this, the efficiency of the system is improved by changing the load angle between the primary and secondary sides. Finally, a 60 kW three-phase IPT system with a DAB is built, and the experimental verification of the study is conducted.

INDEX TERMS Dual active bridge (DAB), inductive power transfer (IPT), zero voltage switching (ZVS).

I. INTRODUCTION

Inductive power transfer (IPT) has the potential to be an important part of the charging infrastructure for electric vehicles (EVs). To meet the requirement of quickly charging EVs, it is necessary to improve the power of IPT systems. At present, the high-power solutions for IPT systems mainly involve series and parallel connections of each part (power module or coupling coils) or three-phase systems [1], [2], [3], [4], [5], [6].

In [7] a thorough review of the current research and outlook of high power wireless charging is presented. It is concluded that multi-phase systems can achieve higher power levels and higher power densities than single-phase systems. In this paper we focus on the three-phase system for IPT.

In addition, zero voltage switching (ZVS), as an important means to improve system efficiency. For ZVS of three-phase systems, most related references are on DC/DC applications [8], [9], [10]. In [8], an asymmetrical duty cycle control strategy is proposed for a three-phase three-level DC/DC converter. To decrease the current stress of switches in high power conditions, a current-tripled-rectifier ZVS three-phase full-bridge DC/DC converter based on a PWM control strategy was proposed in [10].

The dual active bridge (DAB) is an efficient way to achieve ZVS in a three-phase IPT system. DAB has a simple structure, high efficiency and good controllability, and its control method is widely studied in single-phase circuits.

The associate editor coordinating the review of this manuscript and approving it for publication was Alon Kuperman.

DAB control in a three-phase system has also been studied. Reference [11] proposes a novel simultaneous PWM control strategy for a three-phase DAB to realize ZVS in the whole load range.

However, there is a lack of research on ZVS for three-phase IPT systems with DAB. As a high-frequency resonant system, an IPT system has some uniqueness compared with a normal three-phase DC/DC system. The coupling coefficient of IPT system is usually small, which makes the transmitted reactive power significant and affects the efficiency of the system. At the same time, reactive power will change the phase between voltage and current, which is very important for the control of DAB. So the ZVS for three-phase IPT systems with DAB needs to be studied. Nevertheless, there is some research on soft switching with DAB structures in single-phase systems or transformer applications [12], [13], [14], [15], [16].

Article [12] identifies the ZVS switching boundaries for DAB converters by using frequency domain analysis. A triple-phase-shift control strategy for a bidirectional IPT (BIPT) system was proposed in [13] to achieve ZVS for all power switches within the entire power range. A scaled down prototype of 1 kW BIPT system is developed. Paper [14] proposes a dual-side asymmetrical voltage-cancellation control technique for bidirectional IPT systems, which considers both efficiency optimization and zero-voltage switching operation of all switches.

Compared with single-phase system, three-phase system circuit is more complex. The interaction between the phases makes it impossible to achieve the phase shift control like a single-phase system; instead, duty cycle control is used. At the same time, three-phase asymmetry is an additional problem, which does not exist in single-phase systems.

In this paper, a three-phase DAB topology is selected (shown in Fig. 1). The advantages of this topology include employing common three-phase drive inverters, stable DC-link power flow, modular pad design, and zero interphase mutual inductance.

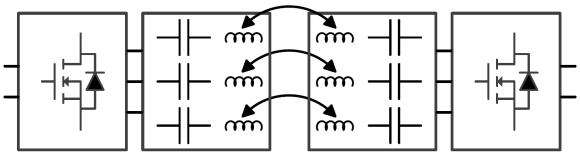

FIGURE 1. Schematic diagram of three-phase DAB IPT system with magnetically decoupled individual pads.

In a three-phase DAB system, there are three degrees of freedom for control. They are the duty cycle of the primary side inverter, the duty cycle of the secondary side inverter, and the switching angle between the primary and secondary sides, which is defined as the load angle in this paper. How to use these control methods to achieve efficient and wide range ZVS power regulation of the three-phase IPT system is the problem to be solved in this paper. The ZVS range of the system with load angle control methods is studied. On this basis, the efficiency of the system is improved by changing the load angle and adjusting the ZVS range of duty cycle control to the full power range.

II. ZVS OF A THREE-PHASE IPT SYSTEM WITH DAB

The ZVS of a bridge circuit is generally realized by having an inductive load, and the DAB topology has the ability to adjust the reflected load impedance. This chapter covers the theoretical conditions to achieve ZVS for a three-phase IPT system with DAB.

A. SINGLE-PHASE AND THREE-PHASE IPT SYSTEM

Fig. 2 is the equivalent circuit diagram of the mutual inductance of the AC side of a single-phase IPT system.

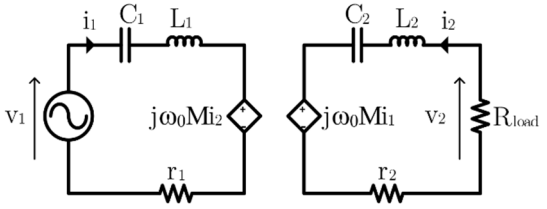

FIGURE 2. Equivalent circuit diagram of the mutual inductance of the AC side of the bidirectional IPT system.

The relationship between the primary and secondary voltage and current can be expressed as

$$\begin{aligned}\dot{V}_1 &= \dot{I}_1(j\omega L_1 - j\frac{1}{\omega C_1}) + j\omega M\dot{I}_2\\ \dot{V}_2 &= \dot{I}_2(j\omega L_2 - j\frac{1}{\omega C_2}) + j\omega M\dot{I}_1.\end{aligned} \tag{1}$$

In a typical IPT system, the inductors and capacitors in the circuit resonate at the operating frequency, i.e., $LC = 1/\omega^2$. From this, (1) can be simplified as

$$\begin{aligned}\dot{V}_1 &= j\omega M\dot{I}_2\\ \dot{V}_2 &= j\omega M\dot{I}_1.\end{aligned} \tag{2}$$

In this case, the inverter has unity power factor.

For three-phase systems, relations (1) and (2) are still valid if the three phases are balanced. The inductance and capacitance in the resonant circuit need to be tuned to meet a certain relationship to maximize the power factor of the system. In fact, there are four basic resonance topologies for the three-phase system (shown in Fig. 3) for both the primary side and secondary side. The relationship between the inductance and capacitance to keep the topologies resonant should follow Table 1.

If the inductors (L_a, L_b, and L_c) in Fig. 3 are coupled with a compensated secondary side, the reflected impedance will be purely resistive and can be put in series with the inductors. In Table 2 the current and voltage stress for L_x and C_x with equal excitation and power transfer is shown. YC-ΔL compensation maximizes the power transfer with minimum voltage stress of the compensation capacitors.

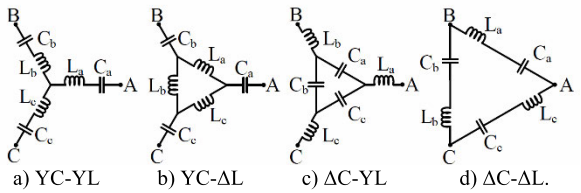

FIGURE 3. Different series connected compensation topologies for three-phase IPT systems.

TABLE 1. Relationship between inductance and capacitance in resonant condition.

Topology	Capacitance	Topology	Capacitance
YC-YL	$C=\frac{1}{\omega^2 L}$	ΔC-YL	$C=\frac{1}{3\omega^2 L}$
YC-ΔL	$C=\frac{3}{\omega^2 L}$	ΔC-ΔL	$C=\frac{1}{\omega^2 L}$

TABLE 2. Component stress for different three-phase series tuning with the same supply voltage and power transfer.

Topology	Voltage stress coil	Voltage stress capacitor	Current stress coil	Current stress capacitor
YC-YL	1	1	1	1
YC-ΔL	$\sqrt{3}$	1	$\frac{1}{\sqrt{3}}$	1
ΔC-YL	1	$\sqrt{3}$	1	$\frac{1}{\sqrt{3}}$
ΔC-ΔL	$\sqrt{3}$	$\sqrt{3}$	$\frac{1}{\sqrt{3}}$	$\frac{1}{\sqrt{3}}$

In these topologies, "YC" has a lower voltage stress but higher current stress on capacitors than "ΔC"; similarly, "YL" has a lower voltage stress but higher current stress on inductors than "ΔL". Considering the limitations of the experimental system, we choose the YC-ΔL topology in this study.

The pads are designed as shown in Fig. 4. Current is the most critical stress factor for the coils due to losses, while voltage stress is the limitation for the compensation capacitors. To reduce both of this, the pads are Δ-connected which will reduce conduction losses and the capacitors are Y-connected to lower the voltage stress. The three-phase system in this study employs a DAB, and the primary and secondary sides of the system exhibit essential symmetry. This enables bidirectional power transmission, similar to other studies utilizing DAB technology [13], [14], [15]. The pads and compensation capacitors are configured according to Table 1 so that any two-phase circuit is in resonance, which contributes to power transfer and soft switching.

Fig. 5 shows a schematic of the primary-side modes of this system. The three digits at the top of Fig. 5 represent the switching states of phases a, b, and c. 1 means the upper switch is on and the lower switch is off, and 0 means the opposite. V_{xp} and I_{xp} represent the output voltage and current of inverter phase x. V_{Cxp} and I_{Lxp} represent the voltage across the compensation capacitor and the coil current. Since the primary and secondary sides are symmetric, the operating modes of the secondary side are not repeated here.

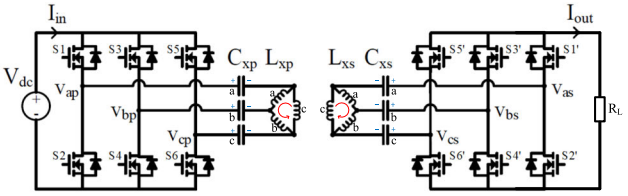

FIGURE 4. Structure of the three-phase IPT system with a DAB.

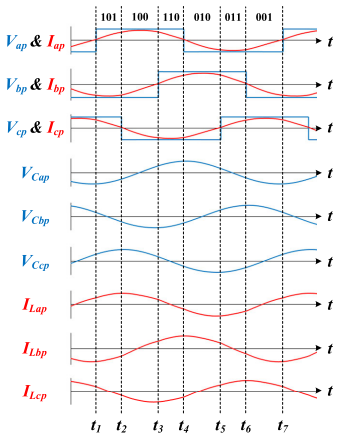

FIGURE 5. Operating modes of three-phase IPT system primary-side.

Although a three-phase IPT system is more complex, its resonance behavior is no different than that of a single-phase system. For instance, based on Fig. 5, Fig. 6 shows the resonance between the a-phase and b-phase bridge legs. "V_{ap} - V_{bp}" and "I_{ap} - I_{bp}" are the phase-to-phase voltage and current. "V_{Cap} - V_{Cbp}" is the sum of the capacitor voltages in the loop and "I_{Lap} - I_{Lbp} - I_{Lcp}" is the sum of the inductor currents in the loop. The energy oscillates back and forth between the inductor and capacitor, leading to the phenomenon of resonance.

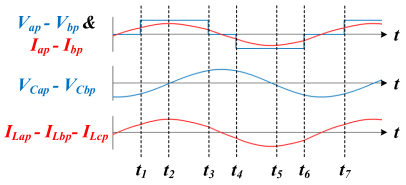

FIGURE 6. Resonance relationship between phases a and b.

With node and mesh analysis of the system in Fig. 4 with YC-ΔL-connection on both sides, the line currents ($i_{\{a,b,c\}}$) and coil currents ($i_{\{1,\ldots,6\}}$) can be expressed as

$$\mathbf{A}x = b \tag{3}$$

$$\begin{bmatrix} \mathbf{A}_{11} & \mathbf{A}_{12} \\ \mathbf{A}_{21} & \mathbf{A}_{22} \end{bmatrix} \begin{bmatrix} i_{\{a,b,c\}p} \\ i_{\{a,b,c\}s} \\ i_{\{1,2,3\}} \\ i_{\{4,5,6\}} \end{bmatrix} = \begin{bmatrix} v_{\{ab,bc,ca\}p} \\ v_{\{ab,bc,ca\}s} \\ 0 \\ 0 \end{bmatrix} \tag{4}$$

where $\mathbf{A}_{ij}$ is 6-by-6 matrices, $\boldsymbol{i}_x$ and $\boldsymbol{v}_x$ are 3-by-1 vectors, and the zero vectors, 0, are 3-by-1. Setting up the node and mesh equations, the A-matrix becomes

$$\mathbf{A}_{11} = \begin{bmatrix} Z_{ap} & -Z_{bp} & 0 & \cdots & 0 \\ 0 & Z_{bp} & -Z_{cp} & \cdots & 0 \\ -Z_{ap} & 0 & Z_{cp} & \cdots & 0 \\ \vdots & \cdots & \cdots & \ddots & \vdots \\ 0 & 0 & 0 & \cdots & Z_{cs} \end{bmatrix} \tag{5}$$

$$\mathbf{A}_{12} = \begin{bmatrix} Z_1 & \cdots & j\omega M_{14} & 0 & 0 \\ 0 & Z_2 & \cdots & j\omega M_{25} & 0 \\ \vdots & \cdots & \ddots & \cdots & \vdots \\ 0 & j\omega M_{52} & \cdots & Z_5 & 0 \\ 0 & 0 & j\omega M_{63} & \cdots & Z_6 \end{bmatrix} \tag{6}$$

$$\mathbf{A}_{21} = \begin{bmatrix} 1 & 0 & \cdots & 0 \\ 0 & 1 & \cdots & 0 \\ \vdots & \cdots & \ddots & \vdots \\ 0 & \cdots & 0 & 1 \end{bmatrix} \tag{7}$$

$$\mathbf{A}_{22} = \begin{bmatrix} -1 & 0 & 1 & 0 & 0 & 0 \\ 1 & -1 & 0 & 0 & 0 & 0 \\ 0 & 1 & -1 & 0 & 0 & 0 \\ 0 & 0 & 0 & -1 & 0 & 1 \\ 0 & 0 & 0 & 1 & -1 & 0 \\ 0 & 0 & 0 & 0 & 1 & -1 \end{bmatrix} \tag{8}$$

where

$$Z_{\{a,b,c\}\{p,s\}} = r_C + 1/(j\omega C_{\{a,b,c\}\{p,s\}})$$

are the compensation capacitor impedances, and

$$Z_{\{1,\ldots,6\}} = r_L + j\omega L_{\{1,\ldots,6\}}$$

are the pad impedances. The subscripts $\{p, s\}$ denotes primary and secondary side respectively. Here the pads are only coupled with a single coil on the other side, which results in a sparse A_{12} matrix. For the general case, the matrix A_{12} is the same as the inductance matrix in (9).

$$\begin{bmatrix} v_1 \\ \vdots \\ v_6 \end{bmatrix} = \begin{bmatrix} j\omega L_{11} + r_1 & j\omega L_{12} & \cdots \\ \vdots & \ddots & \\ j\omega L_{61} & & j\omega L_{66} + r_6 \end{bmatrix} \begin{bmatrix} i_1 \\ \vdots \\ i_6 \end{bmatrix} \tag{9}$$

According to [22], the efficiency-optimized load of an IPT system with series-series compensation can be expressed as

$$R_{L,opt} = \omega M \sqrt{\frac{r_2}{r_1}} \tag{10}$$

Similarly, the per-phase load resistance that maximizes the efficiency of the three phase IPT system in Fig. 4 can be calculated as (10). Since the system is symmetric both electrically and geometrically, the same pad design is used on both sides. Hence, the coil resistances are equal ($r_1 = r_2$)

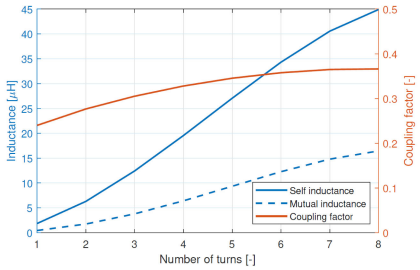

FIGURE 7. Simulation of inductances and coupling for different number of turns. The design of the primary and secondary side is the same.

and (10) simplifies to $R_{L,\text{opt}} = \omega M$. Then the optimal mutual inductance of the system can be expressed as:

$$M_{\text{opt}} = \frac{R_{L,\text{eq}}}{\omega} = \frac{\pi^2}{8} \frac{V_{\text{dc}}^2}{\omega P_{\text{out}}} \tag{11}$$

Considering the trend towards increasing battery voltage, we use a nominal dc-link voltage of 400 V. The targeted power transfer is $P_{\text{out}} = 55$ kW and the resonance frequency is $f_{\text{sw}} = 75$ kHz. This results in a mutual inductance of $M_{\text{opt}} = 7.6\ \mu$H. If the pads are misaligned the mutual inductance will reduce, therefore M_{opt} is a lower boundary for the mutual inductance in the pad design.

In this work the rectangular winding of the pad is selected and the nominal air-gap is 120 mm. The outer dimensions of the pads are limited to 750 mm × 500 mm. Litz wires with a strand diameter of 0.071 mm is selected with a total effective area of 50 mm^2. A finite-element model is developed that has the number of turns, N, as the only free variable. A plot of the self inductances, (L_{xp} and L_{xs}), the mutual inductance, (M_{ps}), and the coupling factor (k_{ps}) for different number of turns is shown in Fig. 7. The number of turns is selected as $N = 5$ which results in a mutual inductance of $M_{\text{ps}} = 9.3\ \mu$H, and self-inductances of $L_{\text{xp}} = L_{\text{xs}} = 27.0\ \mu$H, along with a coupling factor of $k_{\text{ps}} = 0.34$.

The finite element model and the flux density in the ferrite are shown in Fig. 8. The flux is concentrated below the coil and the ferrite in the center is not utilized fully. If weight and cost is a big concern, ferrite can be removed from the center. This will have negligible effect on the coupling factor and losses. Although there will be more stray field behind the pad and additional shielding might be required.

The losses from the inverters are divided into conduction losses and switching losses. Conduction losses are minimized by using synchronous rectification and switching losses are mitigated utilizing ZVS. The principle of synchronous rectification is that the secondary side MOSFETs are turned on in pairs when their respective body diode starts to conduct. The losses for current flowing in the body diode can be calculated as

$$P_{D,\text{loss}} = V_f I_{D(\text{avg})} + r_D I_{D(\text{rms})}^2 \tag{12}$$

where V_f is the diode forward voltage, r_D is the equivalent series resistance of the diode and I_D is the current through

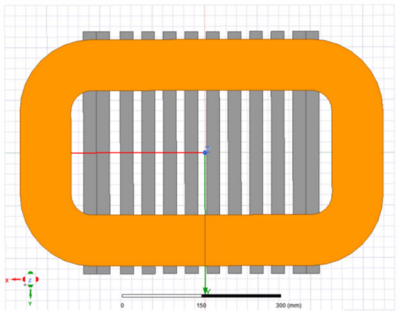

(a) Finite element model of pad

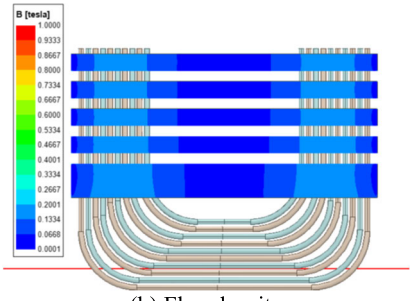

(b) Flux density

FIGURE 8. The finite element simulation model and the flux density distribution in the ferrite.

the diode. Similarly, the losses when current is only going through the channel of the MOSFET can be calculated as,

$$P_{\text{ch,loss}} = r_{\text{ds}} I^2_{\text{ds(rms)}} \tag{13}$$

where r_{ds} is the on-state resistance of the MOSFET and I_{ds} is the current in the channel.

When using synchronous rectification, the current will split between the diode and the channel of the MOSFET. Assuming a sinusoidal secondary side current, $i_2 = i_{\text{ds}} + i_D$, and that the voltage is the same over the channel and the diode,

$$v_{\text{ds}} = i_{\text{ds}} r_{\text{ds}} = i_D r_D + V_f = v_D \tag{14}$$

the expression for $I_{D(\text{avg})}$, $I_{D(\text{rms})}$ and $I_{\text{ds(rms)}}$ becomes

$$I_{D(\text{avg})} = \frac{2\sqrt{2}}{\pi}\left(\frac{I_2 r_{\text{ds}} - V_f}{r_{\text{ds}} + r_D}\right) \tag{15}$$

$$I_{D(\text{rms})} = \frac{I_2 r_{\text{ds}} - V_f}{r_{\text{ds}} + r_D} \tag{16}$$

$$I_{\text{ds(rms)}} = \frac{I_2 r_{\text{ds}} - V_f}{r_{\text{ds}} + r_D} \tag{17}$$

B. INFLUENCE OF THE LOAD ANGLE OF DAB ON ZVS

ZVS in the general sense refers to the addition of an LC resonant circuit outside a switch such that when the LC resonant voltage crosses zero, the switch is turned on to achieve ZVS. The basic principle of ZVS for a MOSFET is to use the energy stored in the inductance at the output of the switch to drain the charge on the parallel capacitor of the switch before the switch is turned on so that the voltage across the switch is zero or slightly negative (with an antiparallel diode on).

For bridge circuits (half-bridges, full bridges, and three-phase bridges), the conditions of ZVS are described as follows: 1. The dead time of the bridge arm is long enough to discharge the capacitor by the inductance of the output terminal; 2. The equivalent load of the bridge arm is inductive (or the current phase lags behind the voltage). The first condition falls under the problem of driving category, which is not covered in this article. The second condition means that the voltage zero crossing point should be earlier than the current zero crossing point, so that the current can discharge the parallel capacitor of the switch before the switch is turned on.

The three-phase bridge switches can be regarded as three independent half-bridge switches because the commutation process of a switch is only related to the current and voltage of its phase. It should be noted that the phase voltage should be used, which has a 30° difference with the line voltage.

In general, inverters of IPT systems often realize soft switching through the slightly inductive impedance of the resonant circuit, but the inductive impedance of the resonant circuit should not be too large, so the range of control (such as phase shift angles or duty cycles) that satisfies the soft switch will be small. For example, when the phase shift angle is decreased to reduce the system power in an H bridge system, it is easy to exceed the range of soft switching.

The control of the load angle can avoid this, so that any phase shift angle or duty cycle can achieve soft switching.

Fig. 9 shows the phase voltages and line currents of both the primary side and secondary side of an IPT system. In the system, the duty of each side and the load angle between both sides can be controlled.

In Fig. 9, $\varphi_l \in [-180°, 180°]$ is the load angle, which is the phase angle between the primary and secondary AC voltage fundamental components. When it is positive, the primary side is the transmitting side, and when it is negative, the primary side is the receiving side. Here we only discuss positive range.

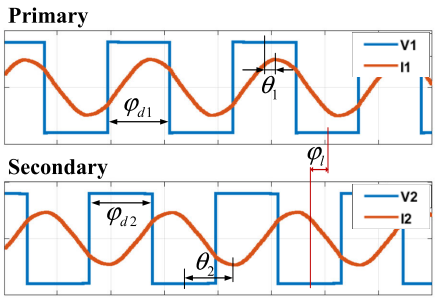

FIGURE 9. Phase voltage and line current of the primary side (top) and secondary side (bottom) in a three-phase DAB, with angle definitions marked (one of three phases is shown).

$\varphi_{d1} \in [0, 360°]$ is the expression of the duty cycle in the angle of the primary side, which is determined by the turn-on duty cycle of the upper leg. When $\varphi_{d1} = 180°$, the conduction time of the upper and lower legs in a cycle each occupies half.

$\varphi_{d2} \in [0, 360°]$ is the expression of the duty cycle in the angle of the secondary side.

$\theta_1 \in [-180°, 180°]$ is the lag angle from the current to the voltage of the primary side. When the primary side is the transmitting side, $\theta_1 \in [-90°, 90°]$. Otherwise, the primary side should be the receiving side.

$\theta_2 \in [-180°, 180°]$ is the lag angle from the current to the voltage of the secondary side.

From the analysis in section II-B, to achieve ZVS, a zero crossing of the current from negative to positive should occur when the voltage is positive; a zero crossing of the current from positive to negative should occur when the voltage is negative. Combined with Fig. 9, the condition for realizing ZVS of the upper leg can be expressed by the inequality

$$\phi_{Vi} - \frac{1}{2}\varphi_{di} \le \phi_{Ii} - 90° \le \phi_{Vi} + \frac{1}{2}\varphi_{di}, (i = 1, 2). \quad (18)$$

where $\emptyset_{Vi}$ and $\emptyset_{Ii}$ are the phases of the voltages and the currents, respectively. The angle difference between them is

$$\phi_{Ii} - \phi_{Vi} = \theta_i, (i = 1, 2). \quad (19)$$

Similarly, for the lower leg, the condition is expressed as

$$\phi_{Vi} + \frac{1}{2}\varphi_{di} \le \phi_{Ii} + 90° \le \phi_{Vi} + 360° - \frac{1}{2}\varphi_{di}, (i = 1, 2). \quad (20)$$

Equations (18) and (19) can be simplified to

$$\begin{cases} 90° - \frac{1}{2}\varphi_{di} \le \theta_i \le 90° + \frac{1}{2}\varphi_{di} \\ \frac{1}{2}\varphi_{di} - 90° \le \theta_i \le 270° - \frac{1}{2}\varphi_{di}. \end{cases}, (i = 1, 2) \quad (21)$$

When the primary side is used as a transmitter and the secondary side is used as a receiver, (20) can be solved to obtain

$$\begin{cases} 180° - 2\theta_1 \le \varphi_{d1} \le 2\theta_1 + 180° \\ 2\theta_2 - 180° \le \varphi_{d2} \le 540° - 2\theta_2. \end{cases} \quad (22)$$

It can be seen from (2) that the phase difference between the current on one side and the fundamental voltage on the opposite side α_0 is always equal to 90°, which means

$$\begin{cases} \theta_1 + \varphi_l = \alpha_0 \\ \theta_2 - \varphi_l = \alpha_0 \\ \alpha_0 = 90°. \end{cases} \quad (23)$$

By combining (22) and (23), we get

$$\begin{cases} 2\varphi_l \le \varphi_{d1} \le 360° - 2\varphi_l \\ 2\varphi_l \le \varphi_{d2} \le 360° - 2\varphi_l \end{cases} \quad (24)$$

as the ZVS operating range of the system, which has solutions only if

$$\varphi_l \le 90°. \quad (25)$$

III. CONTROL METHOD AND ZVS REGION

A. LOAD ANGLE CONTROL

The load angle control controls the power flow by changing the phase-angle of the secondary voltage with respect to the primary side. For a voltage source load with primary and secondary side voltages $\mathbf{v}_1$ and $\mathbf{v}_2$ respectively, the input impedance, $\mathbf{z}_{\text{in}}$, for a tuned series-series compensated system can be expressed as

$$\begin{aligned} \mathbf{z}_{\text{in}} &= \mathbf{v}_1 \frac{r_1 r_2 + \omega^2 M^2}{r_2 \mathbf{v}_1 - j\omega M \mathbf{v}_2} \\ &\approx \omega M \frac{|\mathbf{v}_1|}{|\mathbf{v}_2|} \angle \left(90° - \phi_{12}\right) \end{aligned} \quad (26)$$

The approximation in (26) is valid if $r_1 r_2 \ll \omega M$.

In a similar way the impedance seen from the output can be expressed as

$$\mathbf{z}_{\text{out}} \approx \omega M \frac{|\mathbf{v}_2|}{|\mathbf{v}_1|} \angle \left(90° - \phi_{21}\right) \quad (27)$$

The absolute value of the impedance is constant with respect to ϕ i.e. the amplitude of the currents will be constant. One way to control the system is to choose ϕ such that the active power is maximized, i.e. $\mathbf{z} \in \mathbb{R}$, which is satisfied if ψ is 90 degrees. This will minimize the conduction losses but can cause excessive switching losses since some inductance is necessary to achieve zero-voltage switching.

Based on the analysis in the previous section, a simulation made with load angle control is carried out using PLECS and SIMULINK. The simulation results of output power, ohmic losses (i.e., conduction losses of switches and losses in coils and capacitors) and switching losses are shown in Fig. 10.

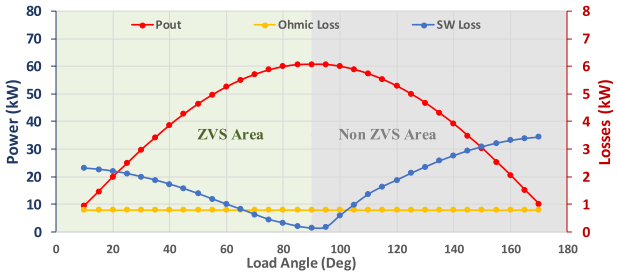

FIGURE 10. Output power, switching losses and ohmic losses at different load angles under load angle control in the simulation (L = 27μH).

It can be seen from the figure that the load angle can significantly change the transmitted power of the system. This is because the change in the load angle changes the angle between the inverter voltage and current and then affects the proportion of active power and reactive power when the total power remains unchanged. When the load angle is 90°, the reactive power is almost zero, and the transmitted power of the system is at the maximum. When the load angle deviates from the 90° point, the reactive power increases and the transmitted power decreases. When the load angle deviates too far, the losses of the system begin to increase significantly.

Moreover, when the load angle is less than 90°, the loss of the system is lower than the symmetry points greater than 90° because the system is in the ZVS area. When the load angle is greater than 90°, the loss of the system gradually increases because the system is in the hard-switching area.

In particular, it should be noted that the load angle significantly affects the switching losses but has no effect on the coil losses, capacitor losses and conduction losses of switching devices, which are summed up as ohmic losses in Fig. 10. The reason why the ohmic losses are practically constant is that the amplitude of the current flowing through the coils, capacitors, and inverters does not change with the change in the load angle.

When the load angle is more than 90°, the system works in a hard switching area, and the switching loss increases rapidly. When the load angle is less than 90°, the system is in the ZVS range, but the switching loss still rises slightly. This is because there is still turn-off loss, which is smaller than the turn-on loss but still considerable when the load angle is small.

The simulation results in ZVS and non-ZVS areas are given in Fig. 11.

To evaluate the influence of the change in coil inductance on the system, a series of simulations were carried out. In the simulations, the coil self-inductance L was changed while keeping the coupling coefficient k and resonant capacitance C unchanged. The results are shown in Fig. 12.

When the inductance changes, the curve of switching losses is shifted because the resonant point changes. The ohmic losses are also affected since the current through coils, capacitors and switching devices is no longer constant.

It can be concluded that the load angle control should be operated in $\varphi_l < 90°$ to change the system power. In this way, the system works in the ZVS area, and the efficiency is higher.

It should be noted that the load angle control in a three-phase IPT system is different from that of a typical three-phase DC-DC converter, because the coupling factor in an IPT system is much smaller than that of a DC-DC converter. This makes the phase difference between the primary and secondary currents in these two systems completely different. In turn, the phase difference is a key element of the load angle control. In addition, the IPT system is difficult to calculate the instant value of the DAB current because the current of DAB is affected by the filter due to the resonance circuit.

B. ASYMMETRICAL DUTY CYCLE CONTROL

Besides the load angle control, the inverter power control of a single-phase IPT system usually uses phase shift control, i.e., changing the phases of the two bridge arms of the H-bridge to control the equivalent voltage of the inverter output. However, this control method is difficult to implement in a three-phase inverter. Because the phase angle is generally fixed at 120 degrees to ensure the three-phase balance. Therefore, another control method of the three-phase DAB system, i.e., asymmetric duty cycle control, is required in order to cooperate with the load angle control. This leads to a difference in the control method between three-phase and single-phase DAB systems.

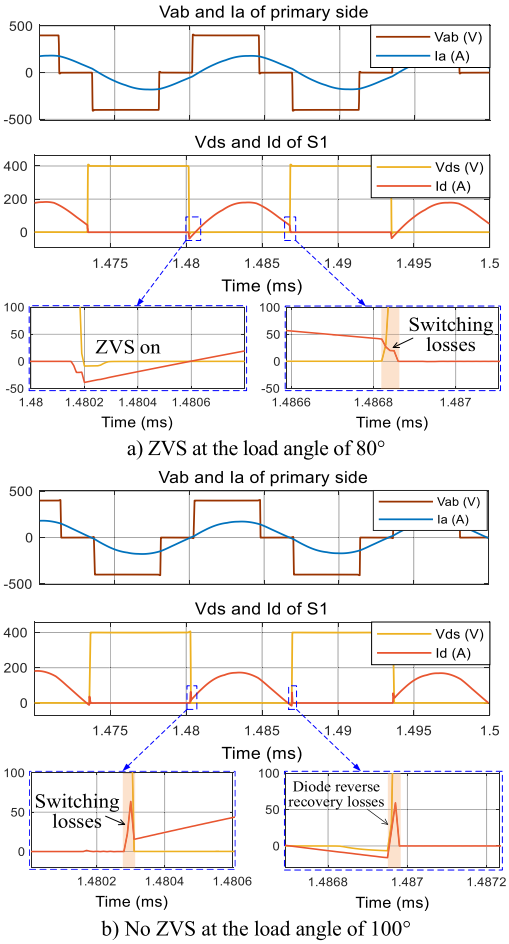

FIGURE 11. Simulation waveforms of the inverter output and MOSFET at different load angles.

In asymmetrical duty cycle control, the duty cycles of the upper and lower switches are complementary, i.e., the sum of the duty cycles in one bridge arm is 100%. The three-phase bridge arms are shifted by 120° to each other. The diagram of gate drivers is shown in Fig. 13, where S1 to S6 are the driving signals of the switch device in Fig. 4.

1) ZVS RANGE OF ASYMMETRICAL DUTY CYCLE CONTROL WITH PASSIVE SECONDARY SIDE

A simulation of asymmetrical control was carried out. The simulation result is shown in Fig. 14. The losses of asymmetrical control in the low power range are lower than those of symmetrical control. The less losses in asymmetrical control are due to the lower current during switching, which makes the switching losses less compared to symmetrical control.

For asymmetric control, as long as the duty cycle is not 50%, the conduction angle of the switch leg will be less than 180°, which will cause the current of the same phase to change sign earlier than the voltage, thereby losing the soft

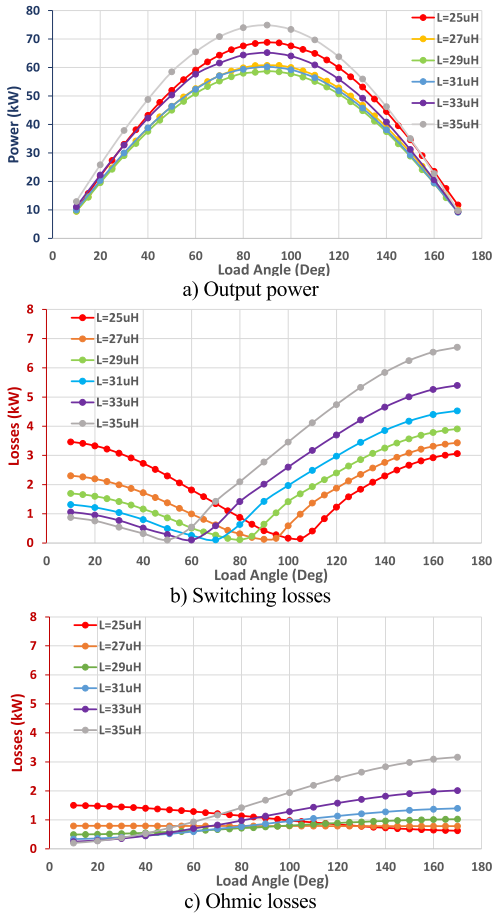

FIGURE 12. System performance that varies with load angle under different coil inductances in simulation.

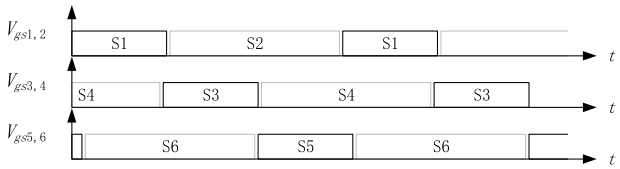

FIGURE 13. Waveform of drivers and output of asymmetrical control.

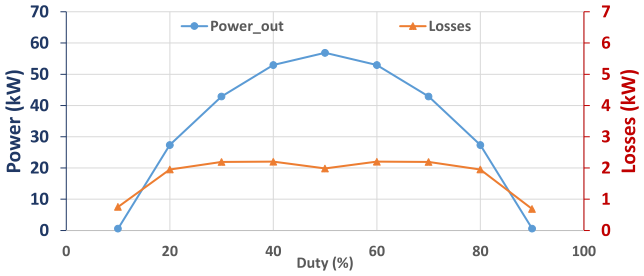

FIGURE 14. Output power and total losses of asymmetrical control in simulation.

switching state. Therefore, under this control method with a resistive load, the system only realizes soft switching when the duty cycle is 50%, that is, the maximum output duty cycle. To achieve soft switching with a smaller duty cycle, the system should be operating with a higher frequency or more inductive load.

2) ASYMMETRICAL CONTROL COMBINED WITH LOAD ANGLE CONTROL

To make the IPT system achieve ZVS in the full power range, the load angle control is combined with duty cycle control. It is important to note that this control is different from both the control of the IPT system with a single-phase DAB structure and the control of the DC-DC converter with a three-phase DAB structure.

Since there are three degrees of freedom, i.e., the load angle and the duty cycle of the primary and secondary sides, there are various ways of such hybrid control. The way chosen in this paper is to keep the duty cycle of the secondary side constant and maximum, and change the load angle and the duty cycle of the primary side. There are two major reasons for the choice: First, the control is simple and only the primary side needs to be controlled. Second, the rectifier conduction angle is always the maximum and the system is able to transmit more power. Fig. 15 shows the phase voltages and line currents of the primary side and secondary side of an IPT system with this kind of hybrid control.

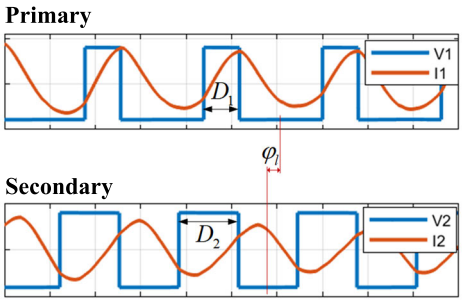

FIGURE 15. Phase voltage and line current in the three-phase IPT system with asymmetrical control combined with load angle control (one of three phases).

To study the characteristics of this control method, a combination of duty cycle and load angle control was carried out in simulations. The simulation uses the system structure shown in Fig. 4 and the system parameters shown in Table 3. The ZVS region of the system obtained from the simulation is shown in Fig. 16. Maps of the output power, efficiency and losses with different duty cycles and load angles are shown in Fig. 17, Fig. 18 and Fig. 19. The output power is symmetric

TABLE 3. Parameters of the constructed system.

Parameter	Value
DC-link voltage	400 V
Output power	60 kW
Coil inductance	27.0 μH
Mutual inductance	9.18μH
Capacitance	500 nF
Coil resistance (ac)	14 mΩ

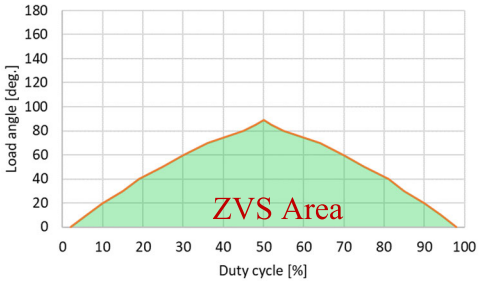

FIGURE 16. Simulation results of the ZVS region of the system under hybrid control.

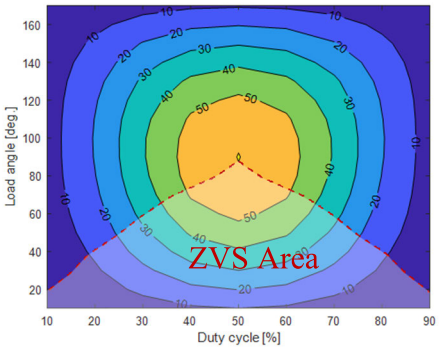

FIGURE 17. Simulated output power with 400 V DC link voltage with combined load angle and asymmetrical duty cycle control. Labels are in kW.

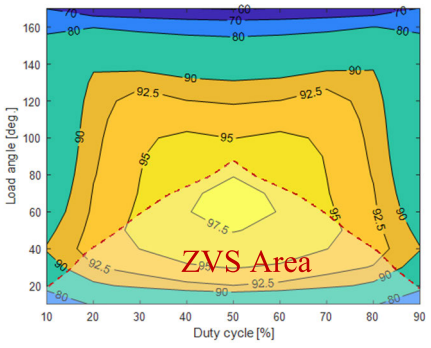

FIGURE 18. Simulated efficiency with 400 V DC link voltage with combined load angle and asymmetrical duty cycle control. Labels are in %.

with respect to both the duty cycle and load angle. The high-efficiency region shifts to the lower load angle range due to the inductive input impedance at the operating frequency ($f_o = 75$ kHz). When the load angle is below 90°, the losses are smaller than when the load angle is above 90° due to lower switching losses.

Due to the complexity of the IPT resonant system, the analytical expression for the ZVS region of the system is not obtained at present, but this does not prevent the feasibility of this hybrid control method.

Although no analytical expression is given for the ZVS region of the system, it is feasible to keep the system

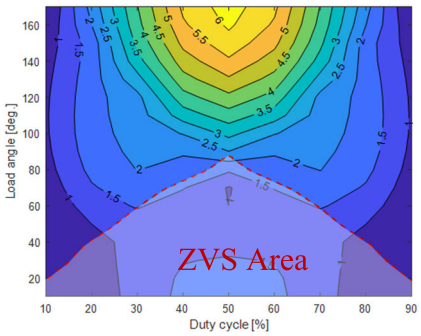

FIGURE 19. Simulated total losses with 400 V DC link voltage with combined load angle and asymmetrical duty cycle control. Labels are in kW.

operating in the ZVS region by control. The implementation is similar to that of synchronous rectification. In the most simplified way, the primary and secondary switching frequencies are set to be the same and the secondary duty cycle is constant at 50%. The primary side only needs to detect the line current cross-zero point of a phase and obtain its current direction at each moment. Then on the basis of duty cycle control, by adjusting the phase angle between the PWM signal and the line current, so that the upper bridge arm turns on when the line current is negative, and the lower bridge arm turns on when the line current is positive. That is, the ZVS of the half bridge of this phase can be guaranteed.

C. THREE-PHASE PHASE-SHIFT REGULATION

When the three-phase loads are unevenly distributed, the currents between phases will be unequal. This leads to unbalanced flow of currents in the system, which can cause equipment overload or overheating. The total power loss in the system will increase, resulting in energy waste and decreased efficiency. To address this issue, phase-shifting control can be implemented to mitigate the imbalance.

In phase-shift control the duty cycle is $d = 50\%$ for all switches. The voltage is instead controlled by phase-shifting the phases. From Fourier analysis the voltage amplitude can be described by

$$\hat{V}_n(\alpha) = \frac{4}{\pi}\frac{V_{\mathrm{dc}}}{n}\sin(\frac{\alpha}{2}) \tag{28}$$

where n is the harmonic order, V_{dc} is the dc-link voltage and α is the phase-shift. From (28), the maximum voltage amplitude is $\hat{V}_{\max} = 4V_{\mathrm{dc}}/\pi$ when $\alpha = 180°$. Phase-shift is often used for controlling power flow in single phase systems but can also be utilized in multi-phase systems.

In a system with m phases the phase-shift should be $\alpha_{\mathrm{sym}} = 2\pi/m$ for symmetric voltages. If $\alpha \neq \alpha_{\mathrm{sym}}$ the voltages will be unbalanced. This can be used to balance the phase-currents if the load is unbalanced.

In this study, phase-shift of the line-voltages are varied according to Fig. 21 and the corresponding amplitudes of the line-voltages are shown in Fig 22. For the case in Fig. 21-d,

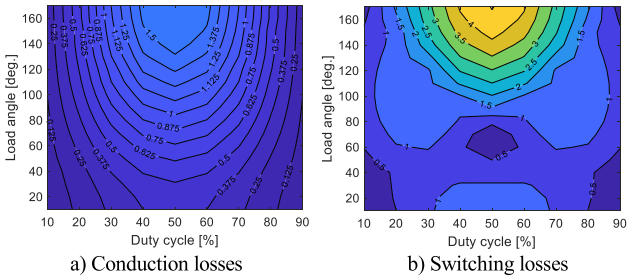

FIGURE 20. Separation of conduction losses and switching losses of the simulation results.

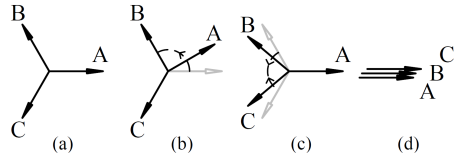

FIGURE 21. Three-phase voltages; (a) 120° symmetric phases (b) one phase-voltage control ∠AB, (c) two phase-voltage control ∠BC, and (d) all voltages in phase.

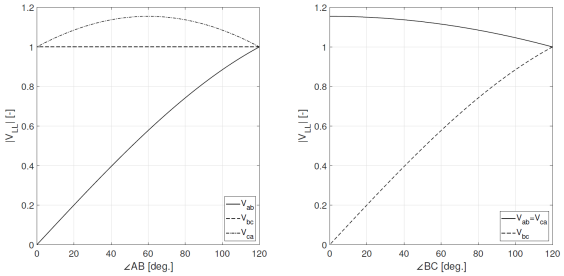

FIGURE 22. Line-voltage amplitudes when phase-shifting ∠AB and ∠BC.

all the line-voltages are zero and therefore no current will flow in this state.

IV. EXPERIMENTAL VERIFICATION

To verify the correctness of the abovementioned theory and simulations, an experimental setup was constructed. The topology of the experimental setup is shown in Fig. 23. To reduce the requirement for DC power supply and limit the dissipated energy, a back-to-back arrangement is used. With this arrangement, only the losses of the system need to be provided from the power supply.

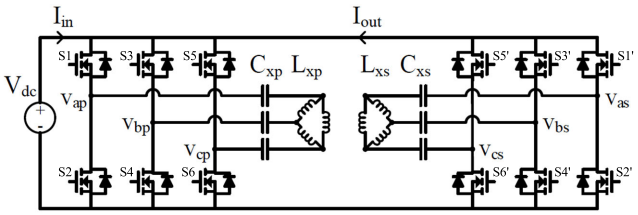

FIGURE 23. Structure of the three-phase IPT system with a DAB. A common DC bus is used to ease the experiments.

A. EXPERIMENTAL SETUP

The three-phase system consists of two three-phase inverters with three Cree-produced 1200 V, 450 A SiC-MOSFET modules (CAB450M12XM3) on both sides. A photo of the setup is shown in Fig. 24, and the electric and parameter values are presented in Table 3.

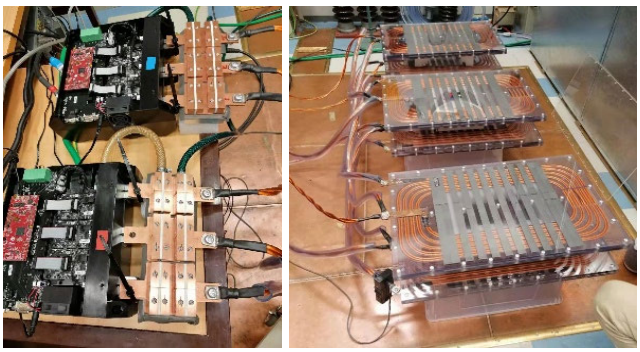

FIGURE 24. The experimental setup.

B. LOAD ANGLE CONTROL

An illustration of the load angle change is shown in Fig. 25. In the top plot, the load angle is 80°, and the zero crossing of the current is just later than the voltage. The voltage waveform has no oscillations, which means that the system is in the ZVS state. When the load angle increases to 90°, as shown in the bottom plot in Fig. 25, the zero-crossing point of the current occurs before the voltage is switched. This gives rise to oscillations in the voltage waveform, which means that the system is in the hard-switching state. This experiment verifies that the load angle control can change the angle between the current and voltage of either side, which affects the ZVS state of the system.

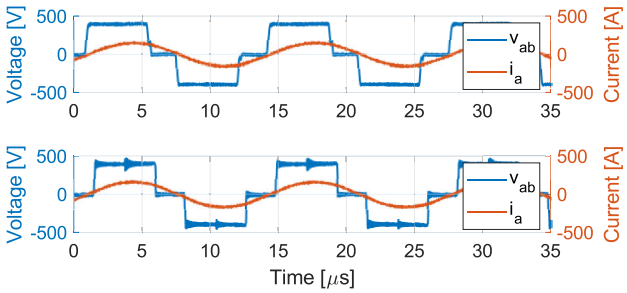

FIGURE 25. Voltage and current waveforms with 80° (upper) and 90° (lower) load angles. At 80°, the system is in the ZVS area, and at 90°, the system is in the non-ZVS area.

In Fig. 26, the turn-on and turn-off are shown with and without ZVS. When the load angle is less than 90°, switching occurs with lower switching losses. When the load angle increases, the MOSFETs enter the non-ZVS state with higher losses. By integrating the product of voltage and current during the switching process, it can be concluded that the

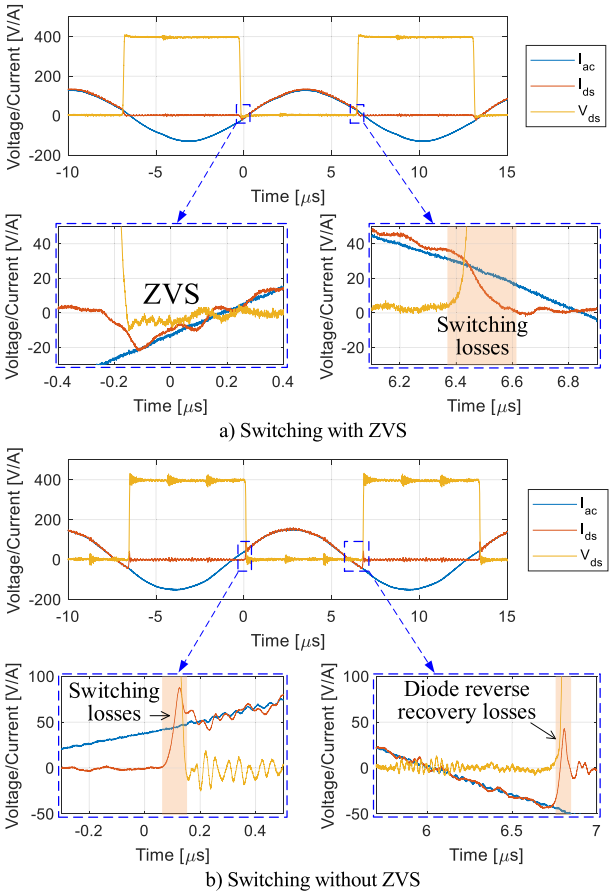

FIGURE 26. Measurements of the switching process with ZVS at smaller load angles (a) and without ZVS at larger load angles (b).

switching energy in Fig. 26-a (the ZVS mode) is about 0.9 mJ, while the switching energy in Fig. 26-b (the non-ZVS mode) is about 2.0 mJ. The switching loss of the ZVS mode in Fig. 26 is half of that of the non-ZVS mode.

An experimental verification of load angle control was carried out. The measurement results are compared with the simulation results (in which $L = 31\ \mu$H) in Fig. 27. The measurements and simulations are in good agreement. The higher coil inductance is presumably due to the long connection cables between coils and capacitors. When the load angle is less than 80°, the system operates in the ZVS area, with a loss of no more than 1.6kW, while when the load angle is greater than 90°, the system operates in the non-ZVS area, with a loss of no less than 2.6kW and up to 6.7kW.

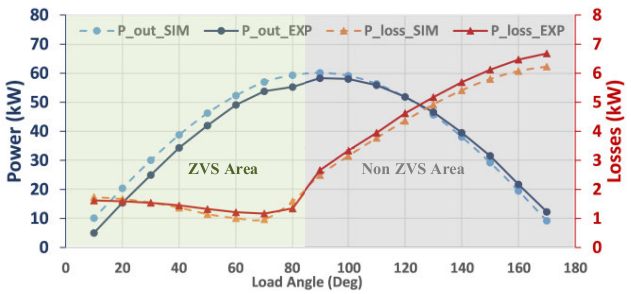

FIGURE 27. Output power and losses for load angle control in simulation (dashed lines) and experiment (solid lines).

C. ASYMMETRICAL DUTY CONTROL

The measurement results of output power and losses for asymmetrical control compared with simulations are shown in Fig. 28.

FIGURE 28. Output power and losses for asymmetrical duty cycle control in simulation (dashed lines) and experiment (solid lines).

In asymmetric control, the simulation and experimental results are almost the same. At the 50% duty point, the loss slightly decreases because the system is in the ZVS state at only this point. In comparison to the load angle control, the asymmetric duty cycle control has more losses in the range of 20kW to 55kW due to operating in a non-ZVS condition. However, when the power is less than 20kW, it will lose less than the load angle control due to the low current stress at low duty cycle, making the hard switching losses insignificant.

D. ASYMMETRICAL CONTROL COMBINED WITH LOAD ANGLE CONTROL

Measurements of the output power, loss and efficiency are shown in Fig. 29, Fig. 30 and Fig. 31, respectively. Comparing with simulation results from Fig. 17, Fig. 18 and Fig. 19, it can

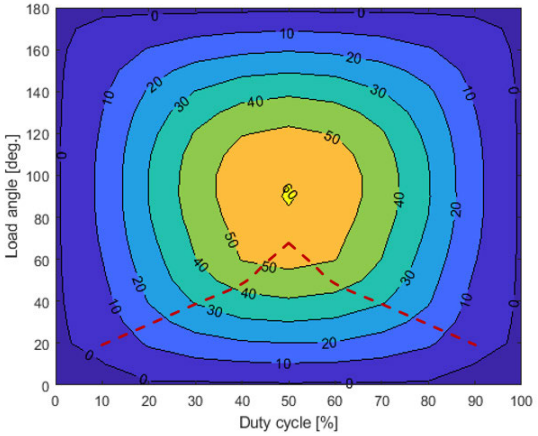

FIGURE 29. Measurements of output power at 400 V DC link voltage with combined load angle and asymmetrical duty cycle control. Labels are in kW. The maximum power is 60 kW at 50% duty cycle and 90° load angle.

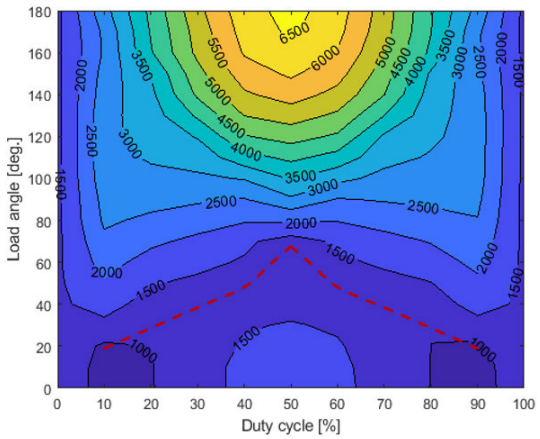

FIGURE 30. Measurements of total losses at 400 V DC link voltage with combined load angle and asymmetrical duty cycle control. Labels are in W. The maximum losses is 6.5kW at 50% duty cycle and 180° load angle, while the losses is 1.5kW at the same duty cycle but zero load angle.

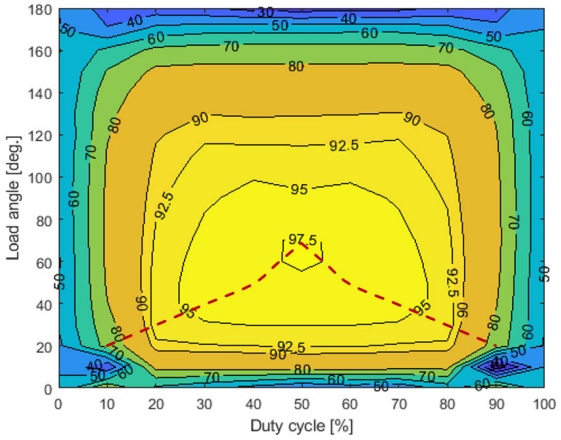

FIGURE 31. Measurements of DC-DC efficiency at 400 V DC link voltage with combined load angle and asymmetrical duty cycle control. Labels are in %. The maximum efficiency can reach 97.5% at 50% duty cycle and 60° load angle.

be concluded that the experimental and simulated maps are similar, which verifies the simulation model.

The red dashed lines in Fig. 29, Fig. 30 and Fig. 31 represent the ZVS boundary of the system in the experiment, and the area below the red line is the ZVS region. It can be seen that compared to the simulation results, both the ZVS region and the high efficiency region of the experimental results are shifted to the lower load angle. The reason is that the inductance of the coil becomes larger due to the presence of a lengthy connection line, similar to that shown in Fig. 12 and Fig. 27.

From the measurements, it can be found that neither load angle control nor duty cycle control alone is the most efficient choice. Power control along the ZVS boundary seems to be a more efficient way of power regulation. Unfortunately, the analytic expressions for the ZVS boundaries are not yet available, which is one of the topics for future research for the three-phase IPT system with a DAB.

V. CONCLUSION

Three-phase IPT with high switching frequency is suitable for high power EV charging. To reduce the losses of a three-phase IPT system, the ZVS operation of a three-phase IPT system with a DAB was studied.

A three-phase IPT system differs from a single-phase IPT system because it cannot use phase-shift control, and it also differs from a three-phase DCDC converter because the loose coupling of the IPT system causes the phase relations between voltages and currents to change.

Based on a three-phase IPT system with a DAB, the conditions for realizing ZVS were discussed. The phase between the AC voltage and current of the converter determines whether it is in the ZVS or non-ZVS area. Experiments show that the switching losses in the ZVS condition are half of those in the non-ZVS condition when the system is operating around full power. The ZVS operating ranges of the system under load angle control and duty control were studied. With a constant DC voltage, the duty control of a three-phase system has a limited ZVS area which is obtained only at maximum power, while by controlling the load angle to be less than 90° the system can be kept within the ZVS area over whole power range. On this basis, the losses of the system were compared for different control methods. Load angle control can achieve lower losses compared to duty cycle control when the system is controlled at 30% to 100% full power. Asymmetrical duty control can be improved by changing the load angle between the primary and secondary sides. Finally, a three-phase IPT setup rated at 60 kW with a DAB was used for experimental verification. The performance of each control method was measured for the complete operating range and compared with theoretical and experimental analysis to verify the correctness of the research.

REFERENCES

[1] J. H. Kim, B.-S. Lee, J.-H. Lee, S.-H. Lee, C.-B. Park, S.-M. Jung, S.-G. Lee, K.-P. Yi, and J. Baek, "Development of 1-MW inductive power transfer system for a high-speed train," *IEEE Trans. Ind. Electron.*, vol. 62, no. 10, pp. 6242–6250, Oct. 2015, doi: 10.1109/TIE.2015.2417122.

[2] J. Pries, V. P. N. Galigekere, O. C. Onar, and G.-J. Su, "A 50-kW three-phase wireless power transfer system using bipolar windings and series resonant networks for rotating magnetic fields," *IEEE Trans. Power Electron.*, vol. 35, no. 5, pp. 4500–4517, May 2020, doi: 10.1109/TPEL.2019.2942065.

[3] H. Hao, G. A. Covic, and J. T. Boys, "A parallel topology for inductive power transfer power supplies," *IEEE Trans. Power Electron.*, vol. 29, no. 3, pp. 1140–1151, Mar. 2014, doi: 10.1109/TPEL.2013.2262714.

[4] X. Fei, Z. Feng, N. PuQi, and W. Xuhui, "Analyzing ZVS soft switching using single phase shift control strategy of dual active bridge isolated DC–DC converters," in *Proc. 21st Int. Conf. Electr. Mach. Syst. (ICEMS)*, Oct. 2018, pp. 2378–2381, doi: 10.23919/ICEMS.2018.8549406.

[5] U. Madawala, D. Thrimawithana, and T. Mouton, "An inductive power tapping (IPT) system for HVDC lines," in *Proc. IEEE 5th Int. Symp. Power Electron. Distrib. Gener. Syst. (PEDG)*, Jun. 2014, pp. 1–5, doi: 10.1109/PEDG.2014.6878645.

[6] B. X. Nguyen, W. Peng, and D. M. Vilathgamuwa, "Multilevel converter topologies based high power inductive power transfer systems," in *Proc. IEEE Int. Conf. Sustain. Energy Technol. (ICSET)*, Nov. 2016, pp. 264–269, doi: 10.1109/ICSET.2016.7811793.

[7] H. Feng, R. Tavakoli, O. C. Onar, and Z. Pantic, "Advances in high-power wireless charging systems: Overview and design considerations," *IEEE Trans. Transport. Electrific.*, vol. 6, no. 3, pp. 886–919, Sep. 2020, doi: 10.1109/TTE.2020.3012543.
[8] F. Liu, Y. Chen, G. Hu, and X. Ruan, "Modified three-phase three-level DC/DC converter with zero-voltage-switching characteristic-adopting asymmetrical duty cycle control," *IEEE Trans. Power Electron.*, vol. 29, no. 12, pp. 6307–6318, Dec. 2014, doi: 10.1109/TPEL.2014.2303655.
[9] D. S. Oliveira and I. Barbi, "A three-phase ZVS PWM DC/DC converter with asymmetrical duty cycle associated with a three-phase version of the hybridge rectifier," *IEEE Trans. Power Electron.*, vol. 20, no. 2, pp. 354–360, Mar. 2005, doi: 10.1109/TPEL.2004.842996.
[10] Z. Shen, K. Jin, C. Liu, C. Wang, and L. Gu, "A current-tripler-rectifier PWM ZVS three-phase full-bridge DC/DC converter with Y-Δ connected transformer," in *Proc. IEEE 5th Int. Symp. Power Electron. Distrib. Gener. Syst. (PEDG)*, Jun. 2014, pp. 1–7, doi: 10.1109/PEDG.2014.6878673.
[11] J. Huang, Y. Wang, Z. Li, Y. Jiang, and W. Lei, "Simultaneous PWM control to operate the three-phase dual active bridge converter under soft switching in the whole load range," in *Proc. IEEE Appl. Power Electron. Conf. Expo. (APEC)*, Mar. 2015, pp. 2885–2891, doi: 10.1109/APEC.2015.7104760.
[12] J. Riedel, D. G. Holmes, and B. P. McGrath, "Identifying ZVS soft switching boundaries for bi-directional dual active bridge DC–DC converters using frequency domain analysis," in *Proc. 9th Int. Conf. Power Electron. ECCE Asia (ICPE-ECCE Asia)*, Jun. 2015, pp. 771–776, doi: 10.1109/ICPE.2015.7167870.
[13] X. Zhang, T. Cai, S. Duan, H. Feng, H. Hu, J. Niu, and C. Chen, "A control strategy for efficiency optimization and wide ZVS operation range in bidirectional inductive power transfer system," *IEEE Trans. Ind. Electron.*, vol. 66, no. 8, pp. 5958–5969, Aug. 2019, doi: 10.1109/TIE.2018.2871794.
[14] S. Jia, C. Chen, S. Duan, and Z. Chao, "Dual-side asymmetrical voltage-cancelation control for bidirectional inductive power transfer systems," *IEEE Trans. Ind. Electron.*, vol. 68, no. 9, pp. 8061–8071, Sep. 2021, doi: 10.1109/TIE.2020.3016265.
[15] Y. Liu, U. K. Madawala, R. Mai, and Z. He, "Zero-phase-angle controlled bidirectional wireless EV charging systems for large coil misalignments," *IEEE Trans. Power Electron.*, vol. 35, no. 5, pp. 5343–5353, May 2020, doi: 10.1109/TPEL.2019.2941709.
[16] R. Ota, D. J. Thrimawithana, U. K. Madawala, and G. A. Covic, "Boundary of soft-switching for efficient operation of bi-directional IPT systems," in *Proc. IEEE PELS Workshop Emerg. Technol., Wireless Power Transf. (WoW)*. Union City, NJ, USA: Wire, Nov. 2020, pp. 164–169, doi: 10.1109/WoW47795.2020.9291279.
[17] M. Hong, G. Xuanjie, Z. Chengbi, and D. Shujiang, "An improved dual phase shift control strategy for dual active bridge DC–DC converter with soft switching," in *Proc. Int. Power Electron. Conf. (IPEC-Niigata-ECCE Asia)*, May 2018, pp. 2718–2724, doi: 10.23919/IPEC.2018.8507524.
[18] H. Hu, T. Cai, S. Duan, X. Zhang, J. Niu, and H. Feng, "An optimal variable frequency phase shift control strategy for ZVS operation within wide power range in IPT systems," *IEEE Trans. Power Electron.*, vol. 35, no. 5, pp. 5517–5530, May 2020, doi: 10.1109/TPEL.2019.2947092.
[19] H. Li, K. Wang, J. Fang, and Y. Tang, "Pulse density modulated ZVS full-bridge converters for wireless power transfer systems," *IEEE Trans. Power Electron.*, vol. 34, no. 1, pp. 369–377, Jan. 2019, doi: 10.1109/TPEL.2018.2812213.
[20] K.-H. Liu and F. C. Y. Lee, "Zero-voltage switching technique in DC/DC converters," *IEEE Trans. Power Electron.*, vol. 5, no. 3, pp. 293–304, Jul. 1990, doi: 10.1109/63.56520.
[21] C. Cui, Y. Liu, D. Pehrman, X. Huang, and Q. Zhang, "A full power range ZVS control technology for bidirectional inductive power transfer system," in *Proc. IECON 46th Annu. Conf. IEEE Ind. Electron. Soc.*, Oct. 2020, pp. 3861–3865, doi: 10.1109/IECON43393.2020.9255256.
[22] D. Pehrman, Y. Liu, C. Cui, and X. Huang, "Loss reduction by synchronous rectification in a 50 kW SiC-based inductive power transfer system," in *Proc. IECON 46th Annu. Conf. IEEE Ind. Electron. Soc.*, Oct. 2020, pp. 3907–3912, doi: 10.1109/IECON43393.2020.9254316.

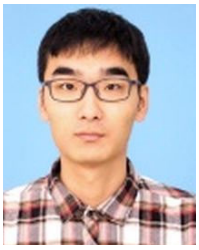

CHAO CUI received the B.Sc. and M.Sc. degrees from the Harbin Institute of Technology, Harbin, China, in 2014 and 2017, respectively, where he is currently pursuing the Ph.D. degree in power electronics.

He is a Visiting Student in inductive charging for electric vehicles with the Department of Electrical Engineering, Chalmers University of Technology. His current research interests include wireless power transfer systems and resonant converters.

DANIEL PEHRMAN (Student Member, IEEE) received the B.Sc. and M.Sc. degrees in electric power engineering from the Chalmers University of Technology, Gothenburg, Sweden, in 2012 and 2014, respectively, where he is currently pursuing the Ph.D. degree in inductive charging for electric vehicles with the Department of Electrical Engineering.

His research interests include inductive power transfer in electric vehicle applications, electric machine design, and power electronic devices.

YUJING LIU (Senior Member, IEEE) received the B.Sc., M.Sc., and Ph.D. degrees in electrical engineering from the Harbin Institute of Technology, Harbin, China, in 1982, 1985, and 1988, respectively.

From 1991 to 1994, he was an Associate Professor of electromagnetic modeling and PM machine design with the Harbin Institute of Technology. From 1996 to 2013, he was with ABB Corporate Research, Västerås, Sweden. Since 2013, he has been a Professor of electric power engineering with the Chalmers University of Technology, Gothenburg, Sweden. His research interests include motors, converters, wireless charging for electric vehicles, generators, power electronics for tidal power conversion, and high-efficiency machines for energy saving in industrial applications.

Dr. Liu is a member of the Swedish Standard Committee on Electrical Machines.

QIANFAN ZHANG (Member, IEEE) was born in Heilongjiang, China. He received the Ph.D. degree in electrical engineering from the Harbin Institute of Technology, Harbin, China, in 2004.

In 1999, he joined the Faculty of the Department of Electrical Engineering, Harbin Institute of Technology, where he has been a Professor, since 2010. His research interests include electric machine and drives, power electronics, integrated charging systems, and wireless power transfer systems applied to electric drive vehicles.